Research Article | Vol. 27, No. 10 | 13 May 2019 | OPTICS EXPRESS 14457
Optics EXPRESS

High-speed collagen fiber modeling and orientation quantification for optical coherence tomography imaging

JAMES P. MCLEAN,[1] YU GAN,[1] THERESA H. LYE,[1] DOVINA QU,[2] HELEN H. LU,[2] AND CHRISTINE P. HENDON[1,*]

[1]*Electrical Engineering, Fu Foundation School of Engineering and Applied Science, Columbia University, 1300 West 120th Street, New York, NY 10025, USA*
[2]*Biomedical Engineering, Fu Foundation School of Engineering and Applied Science, Columbia University, 1300 West 120th Street, New York, NY 10025, USA*
[*]*cpf2115@columbia.edu*

Abstract: Quantifying collagen fiber architecture has clinical and scientific relevance across a variety of tissue types and adds functionality to otherwise largely qualitative imaging modalities. Optical coherence tomography (OCT) is uniquely suited for this task due to its ability to capture the collagen microstructure over larger fields of view than traditional microscopy. Existing image processing techniques for quantifying fiber architecture, while accurate and effective, are very slow for processing large datasets and tend to lack structural specificity. We describe here a computationally efficient method for quantifying and visualizing collagen fiber organization. The algorithm is demonstrated on swine atria, bovine anterior cruciate ligament, and human cervical tissue samples. Additionally, we show an improved performance for images with crimped fiber textures and low signal to noise when compared to similar methods.

1. Introduction

Collagen is the most common matrix component of connective tissue in the human body, providing structural support in a wide variety of organ systems. While the singular collagen fiber provides structure, groups of fibers can facilitate physiological processes. In particular, the organization of collagen fibers has been linked to key mechanical, electrical, and biological functions [1, 2].

Methods for imaging and analyzing collagen fiber organization span many imaging modalities including second harmonic generation (SHG) microscopy [3], diffusion tensor magnetic resonance imaging [4,5], shear wave imaging (SWI) [6], and even histology [7,8]. The challenge in studying collagen's structure-function is that its organization is highly varied on both local and global scales. Optical coherence tomography (OCT) is a valuable tool for studying collagen fiber organization that pairs millimeter field-of-view with micron-scale resolution. OCT has been demonstrated as a useful tool for examining collagen organization in the atrium [9,10], cervix [11], and anterior cruciate ligament (ACL) [12]. Polarization-Sensitive OCT is a functional extension of OCT which can provide enhanced collagen fiber contrast by measuring tissue birefringence. Previous studies have used PS-OCT to visualize collagen organization in fibrous tissue [13, 14]. Paired with Jones or Mueller formalism, local directionality of the tissue can be determined directly from the image [15] and assessed quantitatively via tractography [16, 17].

Collagen organization can be assessed through automatic quantification of fiber orientation. Fleming, et al. developed an iterative approach using intensity-based gradients applied in the *en-face* plane [18]. While their technique provides detail and accuracy, its iterative nature is computationally expensive which can be prohibitive to modeling large fiber networks. Other techniques address this problem using tractography-based methods that operate on the whole image [19, 20]. The improved efficiency, however, is at the expense of specificity because the

#360158 https://doi.org/10.1364/OE.27.014457
Journal © 2019 Received 14 Feb 2019; revised 18 Apr 2019; accepted 24 Apr 2019; published 6 May 2019

Optics EXPRESS

techniques assume dominant contrast in the image originates from collagen fibers which is generally false for *in-vivo* imaging.

Another challenge in fiber quantification, previously identified by Mega, et al., is that fibers may contain orientations which corrupt meaningful analysis, specifically "crimps" [21]. Crimps are a natural feature of tendons and ligaments which are believed to help these tissues resist large strain, but can become accentuated when dehydrated. In OCT images, the crimps cause the collagen fibers to appear scaled with short grooves orientated orthogonally to the fiber itself. Many quantitative fiber orientation algorithms, particularly ones which operate on localized groups of pixels, are unable to differentiate the angles of the crimps from the overall orientation of the fiber.

In this paper, we present a new method for fiber orientation analysis in OCT images. Our method has two components: one which analyzes OCT images to extract a normalized distribution of fiber orientations, and another for visualizations of fibers at specified orientations. We will refer to the quantitative method as the "Radon method" and the visualization method as the "fan-filter method". Our method is validated and tested on OCT images of collagen fibers from bovine ACL, swine atria, and human cervix samples. Additionally, we show a comparison of the proposed method to similar algorithms examining performance, computational efficiency, and robustness to noise and low signal-to-noise (SNR).

2. Methods

2.1. Fiber orientation quantification and visualization

The Radon algorithm for quantifying fiber orientation consists of three primary steps, beginning with the 2D Fast Fourier Transform (FFT). A property of the 2D FFT is that aligned structures in an image produce corresponding alignment in the image spectrum. The algorithm leverages this property to determine the distribution of orientations of aligned structures in the image. For later steps, we also apply an FFT Shift, which inverts the spectrum such that the lowest frequencies are at the center of the image and frequency increases as you move radially away from the center. The second step is to bandpass (BP) filter, which serves multiple purposes. The primary use is to effectively "select" the spatial frequencies of structures of interest. Typically, this means filtering high frequency noise and textures which do not correspond to collagen fiber alignment. The BP filter is also used to filter the DC component (which is typically very large for images) because it contains no orientation information. The final step is to take the Radon Transform of the bandpass filtered image spectrum which converts the orientation information contained in the image spectrum from qualitative to quantitative. The Radon Transform is defined as

$$R\{F(\alpha, s)\} = \int_{-\infty}^{\infty} F(x(z), y(z))dz \tag{1}$$

where, in our case, F is the filtered image spectrum. The pair $(x(z), y(z))$ represent the coordinate parameterization of a straight line with respect to its length L, which is also written as $((z \sin\alpha + s\cos\alpha), (-z\cos\alpha + s\sin\alpha))$. s is the offset between the line and the origin and α is the line's slope. In our case, α is the free variable and s is fixed to the value corresponding to the line passing through the center of the image spectrum. Only the center line is used because of the centered, radially symmetric structure of the 2D FFT. Because only the the center line is used, the algorithm produces not an image, but a single plot. Using an angular resolution of 1°, the Radon method produces a quantitative value for every orientation from 1° to 180° that corresponds to the relative concentration of aligned fibers at that angle. In effect, this can be thought of as an orientation histogram.

The frequency ranges of the bandpass filters employed were $(2.6, 8)\ mm^{-1}$ for the ACL data and $(2.6, 13.4)\ mm^{-1}$ for the atria and cervix datasets. The low frequency cut-off was chosen

Optics EXPRESS

based on physiological knowledge of the expected length of fibers in the image. In general, the high frequency cut-off is chosen to properly filter any high frequency noise, fiber textures, or other small structures in the image which shouldn't contribute to the orientation measurement. The lower high frequency cut-off employed for the ACL images was to filter the crimp pattern, which tends to correspond to spatial frequencies around 10 mm^{-1}.

To create visualizations of the collagen fibers, a series of processing steps are utilized (Fig. 1). The core component of the processing chain is the fan-filter [22]. The fan-filter is defined as a size $N \times N$ array, and is parameterized for each frequency domain pixel location (l, k) based on the minimum and maximum covered angles θ_1, θ_2. More formally, the fan-filter can be written

$$fan(l,k) = \begin{cases} 1 & r = l\cos\theta + k\sin\theta \\ 0 & otherwise \end{cases} \tag{2}$$

where $\theta \in (\theta_1, \theta_2)$ and r is the distance from the center of the image to either edge of the image for a given θ. More intuitively, we can think of the fan-filter as a symmetrical, wedge shaped filter defined by the angles θ_1, θ_2 of the lines which pass through the center of the image and border both edges of the wedge. The result of the fan-filter is that by taking advantage of the rotation property of the 2D FFT, an image with aligned structures can be filtered for a specific range of orientations.

In order to minimize the effect of the Gibbs artifact resulting from the filter's sharp edges, the fan-filter is convolved with a Gaussian window with standard of deviation $\sigma = 0.9$. The fan-filter for a given image is designed based on the range of fiber orientations the user would like to visualize. For the case of a single orientation θ, the fan-filter is designed to have a spread of 20° where $\theta_1 = \theta - 10$ and $\theta_2 = \theta + 10$. After applying the fan-filter to the OCT image, an adaptive thresholding technique is used to create a simple visualization of the fibers. We chose to employ Otsu's method for adaptive thresholding using a sensitivity factor of 0.6. This produces a binary "fiber map" for a particular range of orientations, which can be overlayed in color onto the original OCT image for enhanced visualization.

2.2. Data collection

All images were collected using a commercial, spectral domain OCT system, TELESTO (Thorlabs GmbH, Dachau, Germany) with 6.5 μm axial resolution and 15 μm lateral resolution in air, and a 2.51 mm imaging depth. Immature bovine tibiofemoral joints (4 to 6 months old) were obtained from a local abattoir (Green Village Packing Company) for imaging. Each sample ($N = 4$) comprised the ligament with intact insertion connected to the bone. Multiple three-dimensional data sets of the ACL-to-bone interface were obtained, resulting in four stacks of clear, 4.5 mm by 4.5 mm (900×900 pixel) *en-face* images. Volumetric OCT image sets were also acquired from four swine atrial samples, *ex vivo*. The atrial tissues had been dissected from healthy swine hearts and laid flat for imaging. Cervical samples were acquired and imaged using the process described in [23]. B-scans were reconstructed by processing the raw interferometric data in MATLAB (R2017a, Mathworks).

2.3. Volumetric and mosaic processing

For processing 3D/volumetric image sets and large mosaic images, the fan-filter visualization method is applied in an automatic fashion by leveraging the orientation information calculated by the Radon method. For volumetric data, the fiber orientation distribution is calculated via the Radon method to extract the dominant angle, then the fan-filter visualization is applied using a fan-filter centered at the dominant detected angle. Processing 3D image volumes was accomplished by quantifying the fiber orientation within each *en-face* image at each pixel depth

Optics EXPRESS

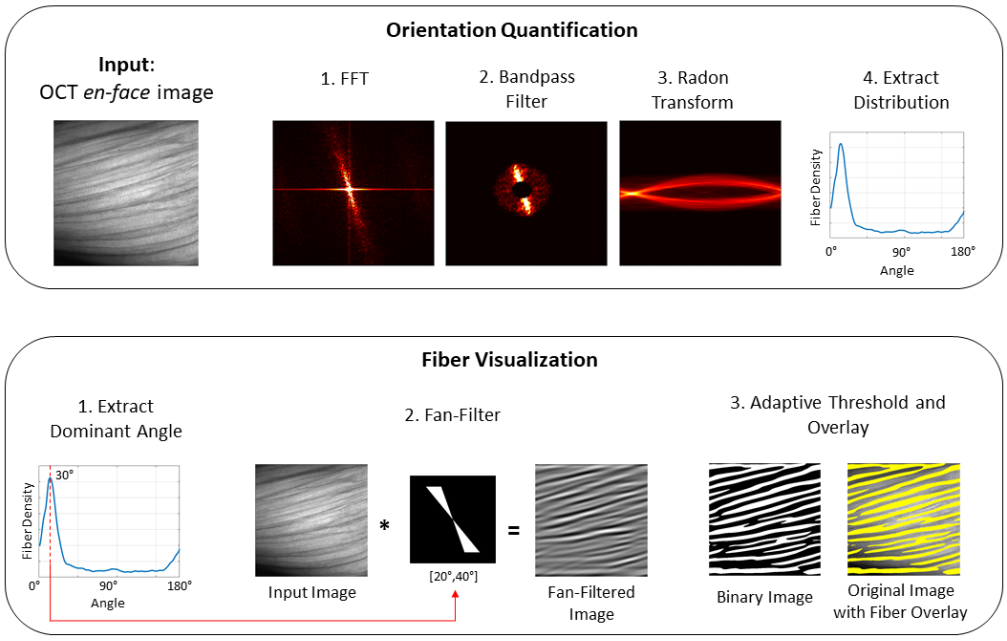

Fig. 1. Flow diagram for fiber orientation quantification and visualization methods. The "Orientation Quantification" method analyzes an en-face OCT image's spectrum to obtain a distribution of the angles of aligned fiber structures in the image. Peaks in the distribution correspond with the dominant fiber angles in the image. The peak angle from the orientation distribution is used to create the "Fiber Visualization". A fan-filter spanning $+/-10^{\circ}$ from the dominant angle is used to filter the OCT image. The result is visualized by applying adaptive thresholding to the fan-filtered image and overlaying the resulting binary image back onto the original OCT image.

of the volume. Each *en-face* image was processed without averaging adjacent planes or taking a segmentation projection.

The automatic visualization process is used in the same fashion for mosaic images, except that the *en-face* plane is divided into 200×200 pixel patches and the method is applied on each patch. This size was chosen based on assessment of the largest area over which local fibers are orientated in a single direction. In general, this "kernel" size should be chosen based on the physiology of the sample being processed. For very large datasets where computational efficiency is important, a filter bank of 180 fan-filters for each possible dominant orientation is precomputed.

2.4. GPU implementation

A GPU implementation of the quantitative fiber orientation method was implemented to further decrease the algorithm's computation time. The majority of the algorithm was implemented using custom CUDA kernels. To efficiently compute the Radon Transform, a GPU implementation from the open-source AstraLabs Toolbox [24] was used.

The GPU implementation of the quantitative fiber orientation method was tested against the CPU version of the method, a region-based gradient method [25], and a pixel-wise method [26] to analyze computational performance. All methods were evaluated on a PC using an Intel(R) Core(TM) i7-6700HQ 2.60 GHz processor and NVIDIA GTX970M GPU. Computational speed as a function of image size was tested on 19 (square) OCT images whose sizes ranged from 100

Optics EXPRESS

x 100 pixels to 1900 x 1900 pixels (0.01 - 3.61 megapixels) in 100 pixel increments.

2.5. Validation

The proposed method was comprehensively validated under a variety of conditions. To start, the method is used to evaluate object orientation in a simulated image with known orientation distribution, and sum-volume images of the ACL where results were compared with manual measure of collagen fiber orientation.

The proposed method is also validated via comparison with two similar algorithms used by our group in previous studies. The first we refer to as the regional or region-based method [25]. This algorithm iteratively evaluates local image intensity gradient in square patches which cover the entire image. Each patch is assigned a single orientation corresponding to the direction of the largest gradient. The other method we refer to as the pixel-wise method [26]. This is another iterative method, but an orientation is assigned to every pixel in the image instead of groups of pixels. Some pixels, however, are assigned no orientation if the local area of that pixel is determined to be isotropic. Both algorithms use two tunable parameters: a threshold for determining whether the local area/pixel is isotropic or anisotropic, and the size of the area being evaluated at each orientation calculation. The thresholds used were 10^{-5} for the regional method and 0.4 for the pixel-wise method. Thresholds were subjectively chosen based on image SNR and reasonable fiber visualization. Window sizes were chosen based on the band-pass filter used in the Radon method for the most accurate comparison between methods. The pixel-wise window was 13 pixels, which corresponds to the spatial frequency of the BP filter's high pass cutoff. The regional method used a window size of 41 pixels, which corresponds to the spatial frequency directly between the low and high pass cutoffs of the BP filter. Both window sizes are also comparable to those used in similar studies [11, 27].

Additional testing was performed to validate algorithm performance in a simulated noise environment and the low signal-to-noise ratio (SNR) environment characteristic of *en-face* images at deep tissue depths. Speckle noise was simulated by first denoising a single *en-face* image from a swine heart sample, and then adding random multiplicative noise. 50 different noise levels were tested with noise variance ranging from 0 to 0.7. The depth sensitivity test was done by simply evaluating algorithm performance for an image volume of the ligament portion of the ACL. The ACL was chosen because fiber orientation in this area is know to be mostly constant with depth [12]. The fiber orientation distribution was measured at every *en-face* image starting at a depth 0.275*mm* from the tissue surface and ending 1.775*mm* deep. For both tests, the results of the radon method are compared with the previously described regional and pixel-wise methods, as well as manual measurements of the dominant angle. The manual measurement is taken for the clean image only, but is compared to the other methods for all noise levels/depths as a way to provide a simple, visual comparison to ground truth.

3. Results

Figure 2 shows results of the orientation quantification method and fan-filter visualization on a synthetic image of a cross (Fig. 2(a)) and an image OCT image of collagen fibers in a bovine ACL sample. For the synthetic image, the fiber orientation distribution produced by the Radon method (Fig. 2(c)) has two distinct peaks which correspond with the orientation of the two bars which form the cross in the image. These two orientations are indicated by the dashed vertical lines at 45° and 135°. The fan-filter visualization (Fig. 2(b)) was generated using two fan-filters centered at 45° and 135°, where the color corresponds to orientation. The same Radon method was applied to a sum volume projection of the ACL to produce the fiber distribution in Fig. 2(e). The dominant orientation of the fibers in the OCT image was also approximated as the average of five manual measurements of orientation at different image locations. This angle is also marked by the vertical dashed line at 26.5° and corresponds nearly perfectly with the peaks

Optics EXPRESS

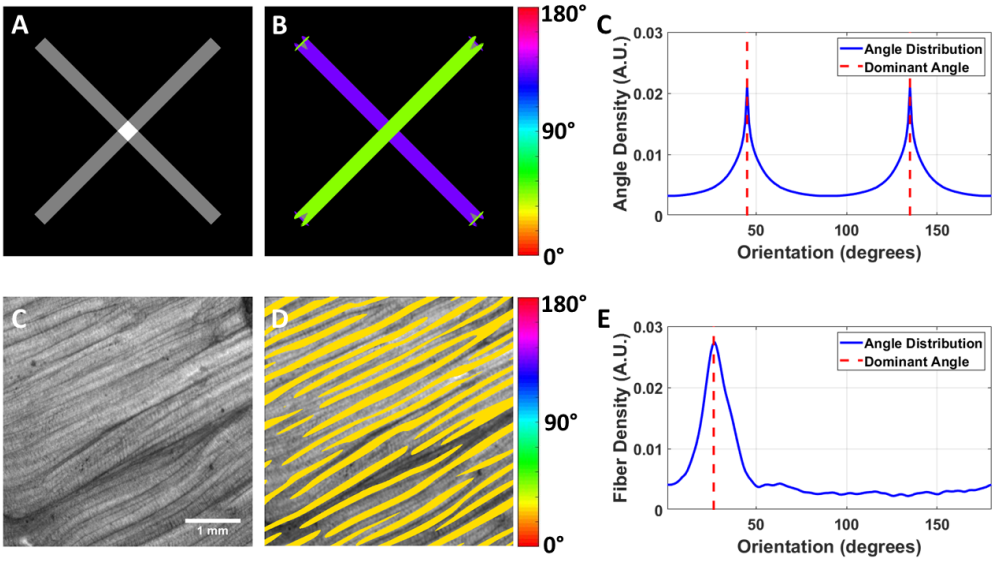

Fig. 2. (a) Synthetic image for validation. (b) Fan-filter visualization of synthetic image. (c) Angular distribution of synthetic image. Dashed red lines mark the true orientation of the overlapping shapes (45° and 135°). (c) *En-face* OCT image of collagen fiber bundles in a bovine ACL sample. (d) Fiber visualization of the OCT image using a 17° to 37° fan-filter. (e) Angular distribution of the OCT image. Dashed red line marks the average fiber orientation determined by manual measurement (26.5°).

of the orientation distribution produced by the Radon method. The fan-filter visualization (Fig. 2(d)) was generated using a single fan filter centered at 26.5°. For additional validation, the orientation quantification method was applied to volumes of the ligament portion of the ACL from four different ACL samples. From those results, the full width at half max (FWHM) of the dominant fiber orientation was calculated, yielding an average alignment deviation of 16.7° across all samples.

Figure 3 compares the fiber orientation analysis of the proposed Radon method with two other similar methods. Both of the other methods take an iterative approach to calculate local orientation in the image space. As suggested by their names, the pixel-wise method assigns an orientation to each pixel in the image, while the regional method does the same for groups of pixels. A visualization of detected fibers and their orientation in Fig. 3(a) is shown for the Radon method (Fig. 3(c)), pixel-wise method (Fig. 3(d)), and regional method (Fig. 3(e)). From visual inspection of the image, we can see that collagen fibers are horizontally aligned. Additionally, the fibers have distinct crimps which run mostly vertically with respect to the image frame.

All three methods are successful at labelling the most distinct fibers with the correct orientation; however, it's clear that in some areas the crimp features dominate and that area is labelled with the crimp orientation instead of the overall fiber orientation. This effect is evident in the fiber distributions shown in Fig. 3(b). The curve in blue was produced by the Radon method while the other two are histograms of the images in Fig. 3(d) and Fig. 3(e). All three curves were normalized to the maximum detected orientation. Looking at each curve, we can see that the pixel-wise method is the most accurate in terms of detecting the dominant fiber distribution. The Radon method has the same dominant angle, and shows it more distinctly than the pixel-wise method, but also has some small peaks around 110° which likely corresponds to the fiber crimps. The regional method also gives the correct dominant angle, but has far fewer total measurements and is significantly more sensitive to the fiber crimping than the other two methods.

Optics EXPRESS

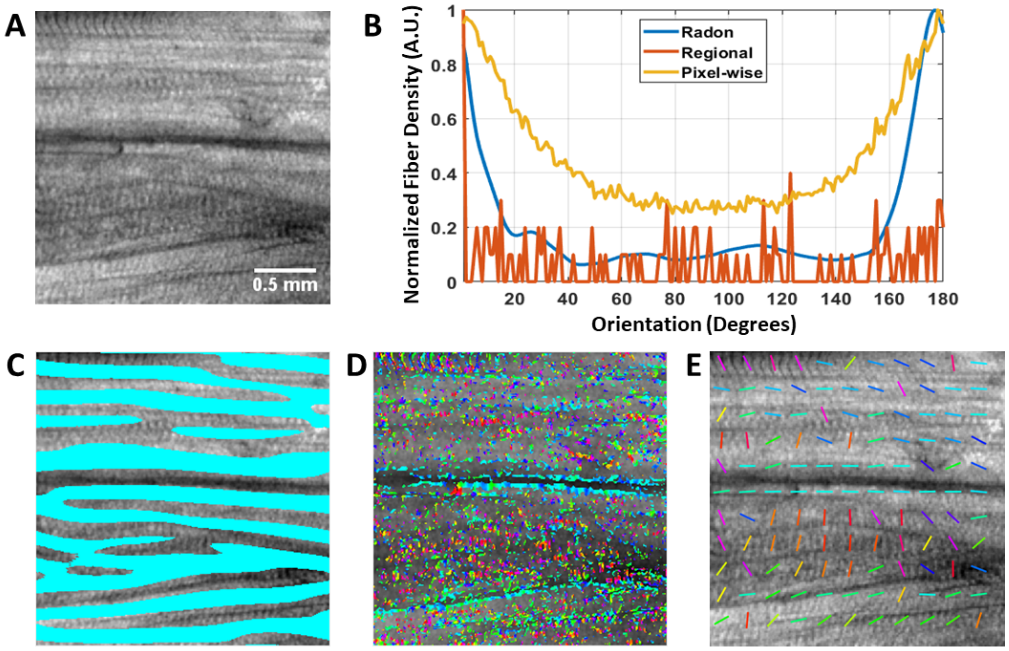

Fig. 3. Fiber visualization results are compared using three different approaches. (a) OCT *en-face* image of collagen fibers in the ligament portion of the ACL. The collagen fibers are horizontally oriented, but have a crimped feature with vertical orientation. (b) Normalized distribution of fiber orientations in (a) using the Radon method, regional method, and pixel-wise algorithm. Fiber visualization results using the Radon/Fan-Filter method (c), the pixel-wise algorithm (d), and regional algorithm (e).

To demonstrate the viability of the algorithm for larger datasets, *en-face* mosaics of a human cervix cross-sectional sample (Fig. 4(a)) and swine left atrium (Figs. 4(c) and 4(d)) were processed. The algorithm was applied iteratively on 200 x 200 pixel patches. At each patch, the fiber distribution was calculated and the patch was fan-filtered using a 20° wide filter centered at the dominant fiber orientation. In the cervix mosaic (Fig. 4(b)), the fiber overlay provides a visualization of the ordered, circular structure of collagen fibers in the outer canal, and the transition to more random alignment at the inner canal, which is in agreement with previous studies [27]. In all the fiber overlays, the fibers are colored according to the dominant angle calculated in the fiber distribution step. To visualize depth-dependent fiber architecture, the fiber visualization method was applied to an image volume of the swine left atrium and insertion region of the ACL. The algorithm was applied to every *en-face* plane and combined into a 3-D image stack (see Visualization 1 and Visualization 2). Figures 4(c) and 4(d) show cross-sections of the swine atrium at the entrance to the pulmonary vein branch at depths of 8.5μm (Fig. 4(c)) and 108.5μm (Fig. 4(d)) below the surface of the tissue. The fiber visualization offers a view of the atrium's depth-dependent fiber architecture. Interestingly, in some areas fiber alignment stays relatively constant in depth (immediately southwest of the entrance to the pulmonary vein branch), while other areas change more rapidly (lower left side of the image). Snapshots of the 3-D model are shown in Figs. 4(e) and 4(f) which were taken from Visualization 1.

Computational efficiency of the Radon method and fan-filter visualization was tested and compared with the regional and pixel-wise methods. Each algorithm was timed on a square image where total computation time was based solely on the algorithm itself, not data loading/saving,

Optics EXPRESS

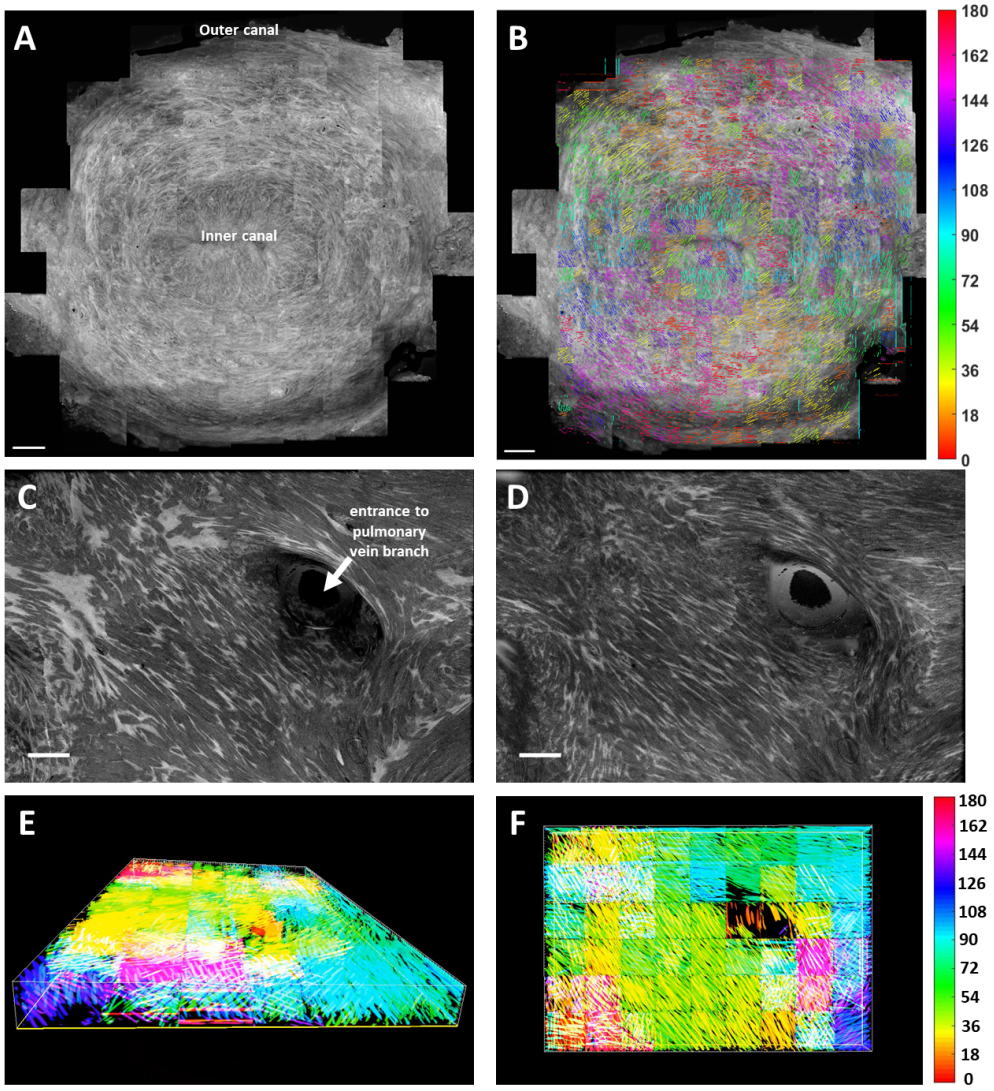

Fig. 4. (a) OCT *en-face* mosaic of human cervix cross-section completely spanning the edges of the outer canal. (b) Collagen fiber visualization created through iterative application of the fan-filter visualization algorithm on 200 x 200 pixel patches and overlaying the result on the original mosaics. (c,d) OCT *en-face* mosaics of a swine left atria cross-section at two different depths separated by $100\mu m$. (e,f) 3-D views of collagen fiber visualization. The visualization method is applied to a stack of *en-face* images to create a 3-D fiber model. Refer to Visualization 1 for a video representation of the 3-D fiber model. Color bars correspond to dominant fiber orientation in the *en-face* plane [0° - 180°]. Scale bars represent 2 mm.

Optics EXPRESS

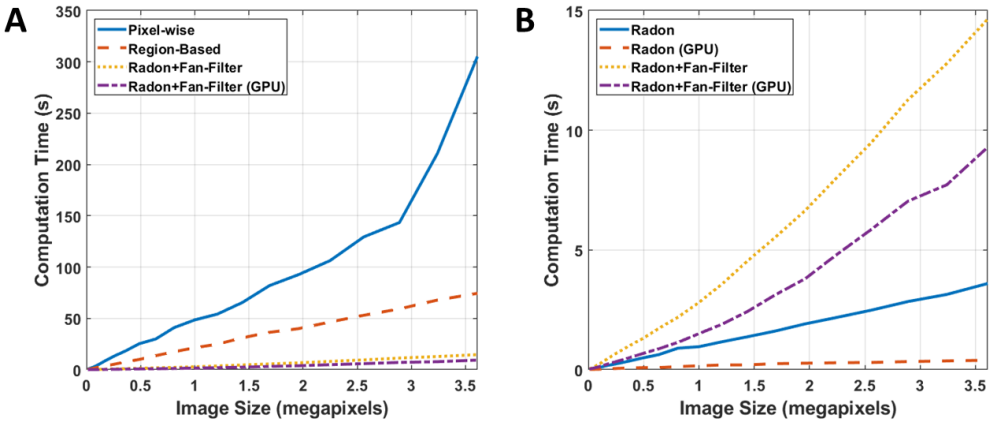

Fig. 5. (a) Computational speed test results for the proposed method, its GPU implementation and two similar methods. Total algorithm computation time was measured for each method and image sizes ranging from 0.01 to 3.61 megapixels. The slowest method was the pixel-wise algorithm, followed by the region-based gradient method. (b) Comparison between Radon method alone, Radon with the fan-filter visualization, and their GPU implementations. The GPU implementation of the Radon method proved to be the fastest at 0.39 seconds for a 3.61 megapixel (1900 x 1900 pixel) image. This is a nearly three orders of magnitude speed-up from the pixel-wise method and an order of magnitude speed-up from the CPU implementation.

pre-processing, or display. In the case of the GPU implementation, the reported times include the algorithm's computation time and the time needed to transfer data back and forth between the GPU and host computer. The results of the test are shown in Fig. 5, where Fig. 5(a) shows the results for all the visualization methods and Fig. 5(b) focuses on the various implementations of the Radon method. The difference in algorithm speed is minimal for small image sizes, but increases dramatically as the image gets larger. Overall, the results go as expected: the slowest are the pixel-wise and regional methods (both iterative approaches) followed by the combined Radon/fan-filter method, then the GPU Radon/fan-filter, the Radon only, and the GPU Radon only. The Radon only versions are reported in addition to the Radon+fan-filter combined method since some applications might not require the fan-filter visualization step (e.g. detecting dominant fiber orientation). Taking a closer look at the times for the one megapixel image, which is closest to the typical size of an *en-face* OCT image, the pixel-wise method took 48.5 seconds, while the Radon+fan-filter method took 1.5 seconds, well beyond an order of magnitude improvement. Comparing to the Radon-only GPU implementation which took 0.16 seconds, the improvement is close to three orders of magnitude.

The performance of the Radon, pixel-wise, and regional methods was tested for an OCT image of the swine left atrium in which speckle noise was artificially added for a normalized noise variance ranging from 0 to 0.7. The cleaned image with no artificial noise is shown in Fig. 6(a) next to the noisiest image in Fig. 6(b). To compare the three algorithms, a distribution of fiber angles was created for the pixel-wise and regional methods by histogramming the detected orientation at each pixel/region of the output image. The dominant angle was chosen as the orientation with the highest count in the histogram. The fiber orientation distributions as a

function of speckle noise variance are shown for the regional (Fig. 6(d)), pixel-wise (Fig. 6(e)), and Radon method (Fig. 6(f)). Each column of the image is the fiber distribution for an image with a particular noise level. The distributions are normalized to the max fiber angle across all noise levels. Figure 6(c) plots the dominant angle for all three algorithms comparing to the manually measured dominant angle (solid line) of 79°.

To quantitatively compare the performance of the three algorithms, average relative error with respect to the manual measurement and standard deviation in the detected dominant angle were calculated at all tested noise levels. The Radon method had the best performance when compared to the manual measurement with an average relative error in dominant angle of 0.98% and standard deviation of 0.3°. The pixel-wise method also performed well with an average relative error of 7.76% and standard deviation of 3.92°. The region based method proved to be significantly more susceptible to noise. The average relative error was 26.4% with a standard deviation of 24.7°

A similar assessment of algorithm performance was applied to an ACL image volume starting at a depth of 0.275 mm (Fig. 6(g)) and ending at 1.775 mm (Fig. 6(h)). Based on the specifications of the imaging system, Fig. 6(g) is representative of depths with a very strong SNR, while Fig. 6(h) has a very poor SNR. Fiber orientation histograms were obtained at each image spanning the depth between 0.275 and 1.775 mm using the regional (Fig. 6(j)), pixel-wise (Fig. 6(k)), and Radon method (Fig. 6(l)). The dominant angle detected by each method is plotted next to the manually measured orientation (75.2°) in Fig. 6(i).

As expected, the test results show that the accuracy of each method decreases with depth. Accuracy was quantitatively evaluated by calculating the standard deviation and relative error in the dominant angle measured by each algorithm. The Radon method had a standard deviation of 1.98 across all depths, much less than the pixel-wise (7.29) and regional (13.9), meaning that the measured dominant angle was more consistent compared to the other methods. Similarly, the average relative error for images deeper than 1 mm was only 6.03% for the Radon method compared to 17.48% for the regional and 30.08% for the pixel-wise method. These results indicate that the regional method could be failing in a different way than the pixel-wise method. The high standard deviation for sub 1 mm images in the regional method suggests that the orientation measurement is being dominated by the speckle noise and is resulting in near random measurements. This is quite different from the pixel-wise method where standard deviation was nearly constant with depth, but the dominant angle seems to "drift" from the manually measured orientation. This seems to suggest that the error in measurement could be the result of the low signal rather than the noise.

4. Discussion

The proposed algorithm provides both a quantitative analysis of fiber distributions in OCT *en-face* images and a corresponding orientation-encoded visualization of those fibers. The results show that the algorithm is successful in quantifying and visualizing fibers of different organ systems, fiber shapes, and SNRs. The algorithm is generally successful in these regimes where others may fail, mostly because both the Radon method and the fan-filter visualization extract orientation information in the frequency domain. This means that filtering steps can be directly implemented into the processing pipeline to not only filter noise, but to also provide structural specificity (like in the case of the crimped ACL fibers).

Ligaments and tendon consist of a highly oriented collagen matrix with characteristic fiber crimp patterns, and this complex matrix organization is a critical determinant of the functional properties of these connective tissues [28, 29]. The dense collagen networks found in healthy tissue typically exhibit a highly aligned architecture along the axis of loading, with a reported alignment deviation of approximately 15° [12, 30, 31]. This is similar to what was observed in this study. Moreover, ligament and tendon tissues have been reported to exhibit a characteristic crimp

Optics EXPRESS

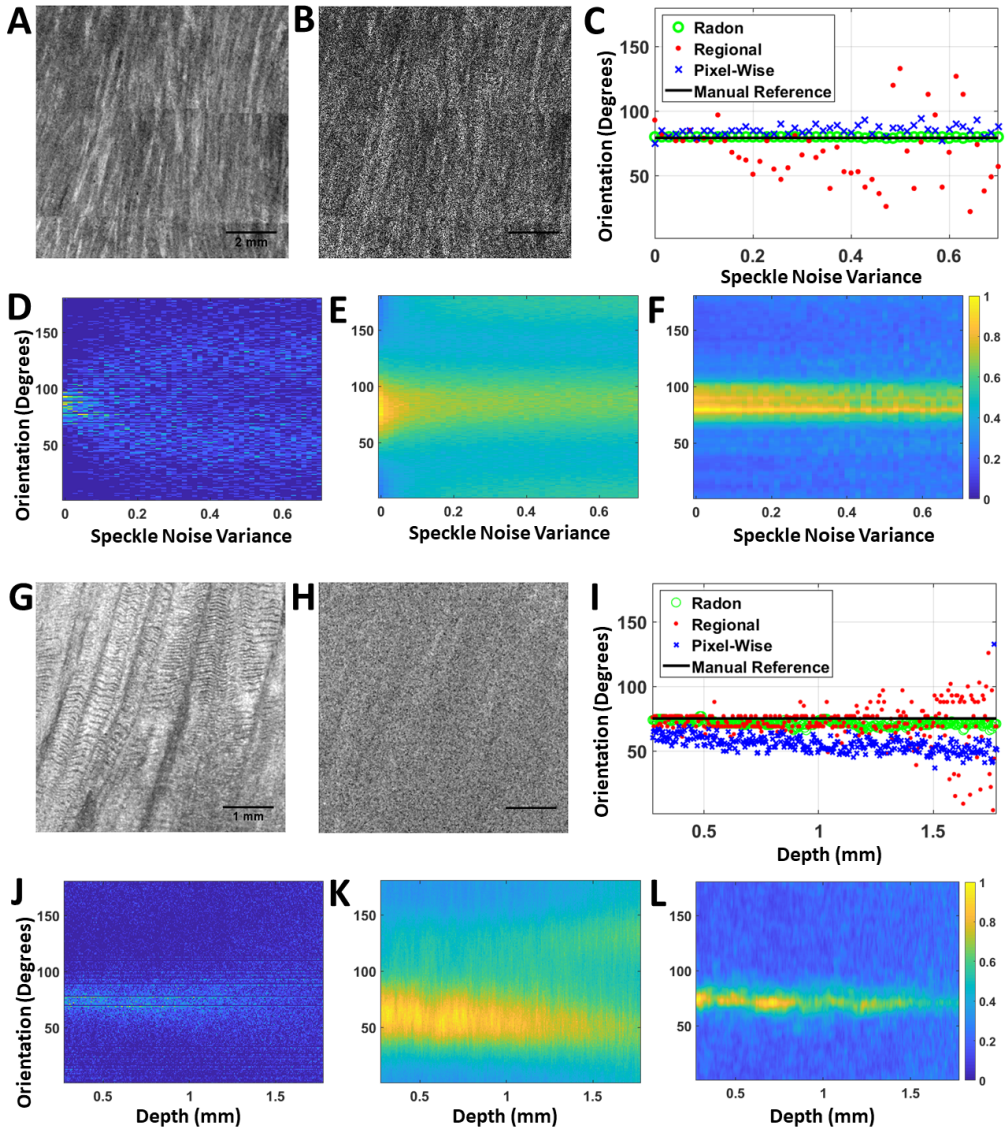

Fig. 6. Noise sensitivity was evaluated by measuring the fiber orientation distribution and dominant fiber angle for a single image with artificially added speckle (multiplicative) noise. (a,b) OCT *en-face* swine left atrium with 0 and 0.7 noise variance, respectively. (c) Dominant angle was measured as a function of noise variance, calculated as the angle corresponding to the max value of the fiber orientation histogram for the regional method (d), pixel-wise method (e), and the radon method (f), was compared against hand-measured ground truth. Sensitivity to depth was analyzed for an ACL image volume spanning a tissue depth of 0.275 mm (g) to 1.775 mm (g). (i) Dominant fiber orientation detected by each algorithm as a function of depth. Fiber orientation histograms were obtained using the regional method (j), pixel-wise method (k), and the radon method (l). In (c) and (i), the dominant angle was manually measured for the images at noise and depth equal to 0, respectively, and is plotted as a visual reference.

Optics EXPRESS

pattern consisting of transverse alternating dark and light bands [32]. In the ACL, this pattern repeats every $45 - 60\mu m$ [33] and, as the tissue is loaded under tension, these crimps appear to flatten and straighten out, thereby acting as a shock absorber during tissue deformation [32, 34].

It is exciting that both collagen fiber organization and the crimp pattern can be observed by OCT imaging and, moreover, quantified via the novel fiber detection algorithm described here. Past studies of collagen matrix organization in ligaments have been largely based on histology images and/or electron microscopy, while OCT enables live imaging of both cell and matrix in a physiologically relevant setting. Findings from this study provide new insights into collagen fiber organization and serve as benchmark criteria for successful tissue regeneration.

The Radon-based fiber orientation method was designed to closely resemble the method proposed by Mega, et al for Second Harmonic Generation Microscopy images [21]. The primary goal in this study was to create a method for quantifying and visualizing fiber orientation as fast as possible without significant sacrifices in accuracy. We felt the Radon method was best suited to this task because its Fourier-based approach offered simplicity, robustness, and efficiency to the task in a way other algorithms did not. Two steps from Mega's method which were removed to further improve the speed of the method were histogram equalization and median filtering of the image spectrum, which we found to have minimal effect on the detection of the dominant fiber angle. This was advantageous towards decreasing computation time because the resulting method was completely linear.

Fan-filters are also not a new idea; however, to the best of our knowledge, there have been no published works which apply them to the task of fiber visualization. Furthermore, the idea of combining fan-filters with a fiber orientation detection algorithm in order to automate fiber visualization processing for very large image volumes or mosaics is a completely novel application of these methods. There are also many ways in which the fan-filter visualization step can be improved. Significant work has been (and continues to be) devoted to efficient and accurate design of 2-D FIR fan-filters [22, 35–37]. The method we chose for creating the fan-filters is fast and flexible, but by no means produces a filter with benefits of a true FIR design. While not very simple to implement, employing design strategies like that proposed by Bindima, et al. will likely increase the accuracy of the fiber visualization. Another area for improvement is processing image volumes and mosaics of heterogeneous tissues. Currently, the method assumes that every image consists mostly of fibers and that SNR is high enough to resolve them. In future work, detection criteria can be incorporated to determine which areas have fibers so that the process can be further automated.

To the best of our knowledge, algorithm performance in the presence of noise or in low SNR regions has not been previously examined in other studies proposing similar methods. The motivation for assessing algorithm performance under these conditions is that they are not only prevalent, but largely unavoidable in OCT imaging. While a plethora of OCT denoising techniques have been proposed, the most effective techniques can take many second to process a single image which is prohibitive to any real-time processing task where processing time needs to be on the order of milliseconds [38, 39]. We felt that to propose an algorithm for processing OCT images that could work real-time it needed to be robust enough to noise and poor SNR that lengthy pre-processing steps would be unnecessary. To this end, the results of the noise test were encouraging. For both the simulated noise case and the low SNR case, the Radon method produced consistent and accurate results, especially for the task of the measuring the dominant fiber angle. Based on this assessment, the Radon method should be capable of reliably measuring fiber orientation in OCT images as deep as 1.5 mm below the tissue surface.

To our knowledge, the Radon and fan-filter combined method for quantifying and visualizing collagen fiber orientation is the fastest of such algorithms to be proposed. The results of the computational efficiency test (Fig. 5) demonstrate this improvement which is even further improved with larger images. When choosing a particular fiber orientation and visualization

Optics EXPRESS

method, there is always some trade-off between computational efficiency and accuracy. Based on the performance comparison (Fig. 3) and the computational efficiency test (Fig. 5), it's clear that the pixel-wise method sacrifices speed for precision and detail, the proposed Radon method has the opposite trade off, and the regional method lies somewhere inbetween the two.

Ultimately, the best choice of algorithm depends on the application. When analyzing samples with high local variability in tissue structure and when capturing all the detail of the fiber architecture is important, then pixel-wise methods are likely most appropriate. If the application only requires determining the dominant fiber orientation over a large area and the fiber architecture is not too complex, then the Radon method is probably sufficient. Although only demonstrated for OCT, the Radon Method is not specific to any imaging modality and could be used to improve fiber analysis in PS-OCT as well. The novelty of the Radon method combined with the fan-filter fiber visualization is that the computational efficiency is so improved compared to other methods that new applications for collagen fiber characterization may now be possible. As an *in-vivo* imaging technique, OCT particularly benefits from analysis which can be performed real time. In the future, we hope this method can be used to assist in real time analysis of fiber architecture for dynamic imaging tests such as analyzing the ACL during leg inflection, a pumping heart, or stretching of the cervix and uterus during pregnancy.

5. Conclusion

In this manuscript, an algorithm was presented for quantitative fiber orientation analysis and visualization in *en-face* OCT images. The method was validated against similar algorithms and manual measurement, for various samples including swine heart, bovine ligament, and human cervical tissue, and for images with low SNR and high speckle noise variance. We found the proposed algorithm to be less susceptible to uninformative orientations produced by fiber crimping and speckle noise, and was capable of obtaining reliable measurements of dominant fiber orientation from areas deeper in tissue when compared with similar methods. Most notably, the proposed method was significantly more computationally efficient than other iterative techniques. A GPU implementation of the technique was implemented resulting in an order of magnitude improvement in computation time. In future work, we hope to incorporate this method into an OCT system for real time measurement and visualization of collagen fiber orientation.

Funding

Department of Defense (W81XWH-15-1-0685); National Science Foundation (CAREER Award 1454365); National Institutes of Health (R01-AR055280, 1DP2HL127776-01).

References

1. T. H. Lye, K. P. Vincent, A. D. McCulloch, and C. P. Hendon, "Tissue-specific optical mapping models of swine atria informed by Optical Coherence Tomography," Biophys. J. **114**, 1477–1489 (2018).
2. R. Zareian, M. E. Susilo, J. A. Paten, J. P. McLean, J. Hollmann, D. Karamichos, C. S. Messer, D. T. Tambe, N. Saeidi, J. D. Zieske, and J. W. Ruberti, "Human corneal fibroblast pattern evolution and matrix synthesis on mechanically biased substrates," Tissue Eng. Part A **22**, 1204–1217 (2016).
3. F. J. Avila and J. M. Bueno, "Analysis and quantification of collagen organization with the structure tensor in second harmonic microscopy images of ocular tissues," Appl. Opt. **54**, 9848–9854 (2015).
4. M. Eggen, C. Swingen, and P. Iaizzo, "Analysis of fiber orientation in normal and failing human hearts using diffusion tensor MRI," in *2009 IEEE International Symposium on Biomedical Imaging: From Nano to Macro,* (IEEE, 2009), pp. 642–645.
5. H. Yan, O. Carmichael, D. Paul, and J. Peng, "Estimating fiber orientation distribution from diffusion MRI with spherical needlets," Med. Image Anal. **46**, 57–72 (2018).
6. W. N. Lee, M. Pernot, M. Couade, E. Messas, P. Bruneval, A. Bel, A. A. Hagège, M. Fink, and M. Tanter, "Mapping myocardial fiber orientation using echocardiography-based shear wave imaging," IEEE Trans. Med. Imaging **31**, 554–562 (2012).

Optics EXPRESS

7. T. B. Leergaard, N. S. White, A. de Crespigny, I. Bolstad, H. D'Arceuil, J. G. Bjaalie, and A. M. Dale, "Quantitative histological validation of diffusion MRI fiber orientation distributions in the rat brain," PLoS ONE **5**, 1–8 (2010).
8. K. G. Schilling, V. Janve, Y. Gao, I. Stepniewska, B. A. Landman, and A. W. Anderson, "Histological validation of diffusion MRI fiber orientation distributions and dispersion," Neuroimage **165**, 200–221 (2018).
9. C. M. Ambrosi, V. V. Fedorov, R. B. Schuessler, A. M. Rollins, and I. R. Efimov, "Quantification of fiber orientation in the canine atrial pacemaker complex using optical coherence tomography," J. Biomed. Opt. **17**, 071309 (2012).
10. C. Fan and G. Yao, "Imaging myocardial fiber orientation using polarization sensitive optical coherence tomography," Biomed. Opt. Express **4**, 460–465 (2013).
11. K. M. Myers, C. P. Hendon, Y. Gan, W. Yao, K. Yoshida, M. Fernandez, J. Vink, and R. J. Wapner, "A continuous fiber distribution material model for human cervical tissue," J. Biomech. **48**, 1533–1540 (2015).
12. D. Qu, P. J. Chuang, S. Prateepchinda, P. S. Balasubramanian, X. Yao, S. B. Doty, C. P. Hendon, and H. H. Lu, "Micro- and ultrastructural characterization of age-related changes at the anterior cruciate ligament-to-bone insertion," ACS Biomater. Sci. Eng. **3**, 2806–2814 (2017).
13. E. Li, S. Makita, Y.-J. Hong, D. Kasaragod, and Y. Yasuno, "Three-dimensional multi-contrast imaging of in vivo human skin by Jones matrix optical coherence tomography," Biomed. Opt. Express **8**, 1290–1305 (2017).
14. J. Walther, Q. Li, M. Villiger, C. S. Farah, E. Koch, K. Karnowski, and D. D. Sampson, "Depth-resolved birefringence imaging of collagen fiber organization in the human oral mucosa in vivo," Biomed. Opt. Express **10**, 1942–1956 (2019).
15. N. Ugryumova, J. Jacobs, M. Bonesi, and S. J. Matcher, "Novel optical imaging technique to determine the 3-D orientation of collagen fibers in cartilage: variable-incidence angle polarization-sensitive optical coherence tomography," Osteoarthr. Cartil. **17**, 33–42 (2009).
16. Y. Wang and G. Yao, "Optical tractography of the mouse heart using polarization-sensitive optical coherence tomography," Biomed. Opt. Express **4**, 2540–2545 (2013).
17. L. Azinfar, M. Ravanfar, Y. Wang, K. Zhang, D. Duan, and G. Yao, "High resolution imaging of the fibrous microstructure in bovine common carotid artery using optical polarization tractography," J. Biophotonics **10**, 231–241 (2017).
18. C. P. Fleming, C. M. Ripplinger, B. Webb, I. R. Efimov, and A. M. Rollins, "Quantification of cardiac fiber orientation using optical coherence tomography," J. Biomed. Opt. **13**, 030505 (2008).
19. J. A. Germann, E. Martinez-Enriquez, and S. Marcos, "Quantization of collagen organization in the stroma with a new order coefficient," Biomed. Opt. Express **9**, 173–189 (2018).
20. C. J. Goergen, H. Radhakrishnan, S. Sakadžic, E. T. Mandeville, E. H. Lo, D. E. Sosnovik, and V. J. Srinivasan, "Optical coherence tractography using intrinsic contrast," Opt. Lett. **37**, 3882–3884 (2012).
21. Y. Mega, M. Robitaille, R. Zareian, J. McLean, J. Ruberti, and C. DiMarzio, "Quantification of lamellar orientation in corneal collagen using second harmonic generation images," Opt. Lett. **37**, 3312–3314 (2012).
22. E. Z. Psarakis, V. G. Mertzios, and G. P. Alexiou, "Design of two-dimensional zero phase FIR fan filters via the McClellan transform," IEEE Trans. Circuits Syst. **37**, 10–16 (1990).
23. Y. Gan, W. Yao, K. M. Myers, J. Y. Vink, R. J. Wapner, and C. P. Hendon, "Analyzing three-dimensional ultrastructure of human cervical tissue using optical coherence tomography," Biomed. Opt. Express **6**, 1090–1108 (2015).
24. W. van Aarle, W. J. Palenstijn, J. Cant, E. Janssens, F. Bleichrodt, A. Dabravolski, J. De Beenhouwer, K. Joost Batenburg, and J. Sijbers, "Fast and flexible X-ray tomography using the ASTRA toolbox," Opt. Express **24**, 25129–25147 (2016).
25. Y. Gan and C. P. Fleming, "Extracting three-dimensional orientation and tractography of myofibers using optical coherence tomography," Biomed. Opt. Express **4**, 2150–2165 (2013).
26. K. P. Quinn and I. Georgakoudi, "Rapid quantification of pixel-wise fiber orientation data in micrographs," J. Biomed. Opt. **18**, 046003 (2013).
27. W. Yao, Y. Gan, K. M. Myers, J. Y. Vink, R. J. Wapner, and C. P. Hendon, "Collagen fiber orientation and dispersion in the upper cervix of non-pregnant and pregnant women," PLoS ONE **11**, 1–20 (2016).
28. F. H. Silver, J. W. Freeman, and G. P. Seehra, "Collagen self-assembly and the development of tendon mechanical properties," J. Biomech. **36**, 1529–1553 (2003).
29. C. J. Stender, E. Rust, P. T. Martin, E. E. Neumann, R. J. Brown, and T. J. Lujan, "Modeling the effect of collagen fibril alignment on ligament mechanical behavior," Biomech. Model. Mechanobiol. **17**, 543–557 (2018).
30. P. Whittaker and P. B. Canham, "Demonstration of quantitative fabric analysis of tendon collagen using two-dimensional polarized light microscopy," Matrix **11**, 56–62 (1991).
31. T. Y. Lau, R. Ambekar, and K. C. Toussaint, "Quantification of collagen fiber organization using three-dimensional Fourier transform-second-harmonic generation imaging," Opt. Express **20**, 21821–21832 (2012).
32. M. Franchi, V. Ottani, R. Stagni, and A. Ruggeri, "Tendon and ligament fibrillar crimps give rise to left-handed helices of collagen fibrils in both planar and helical crimps," J. Anat. **216**, 301–309 (2010).
33. C. T. Laurencin and J. W. Freeman, "Ligament tissue engineering: An evolutionary materials science approach," Biomaterials **26**, 7530–7536 (2005).
34. M. Franchi, M. Fini, M. Quaranta, V. De Pasquale, M. Raspanti, G. Giavaresi, V. Ottani, and A. Ruggeri, "Crimp morphology in relaxed and stretched rat Achilles tendon," J. Anat. **210**, 1–7 (2007).
35. S. Pei and J. Shyu, "Design of 2D FIR digital filters by McClellan transformation and least squares eigencontour mapping," IEEE Trans. Circuits Syst. II Analog. Digit. Signal Process. **40**, 546–555 (1993).

Optics EXPRESS

36. W. Zhu and S. Nakamura, "An efficient approach for the synthesis of 2-D recursive fan filters using 1-D prototypes," IEEE Trans. Signal Process. **44**, 979–983 (1996).
37. T. Bindima, U. K. Shahanas, and E. Elias, "Low complexity fan filters using multiobjective artificial bee colony optimization aided McClellan Transformation for directional filtering," IEEE Trans Circuits Syst II Express Briefs **65**, 2057–2061 (2018).
38. K. Dabov, A. Foi, V. Katkovnik, and K. Egiazarian, "Image denoising by sparse 3-D transform-domain collaborative filtering," IEEE Trans. Image Process. **16**, 2080–2095 (2007).
39. C. Cuartas-Vélez, R. Restrepo, B. E. Bouma, and N. Uribe-Patarroyo, "Volumetric non-local-means based speckle reduction for optical coherence tomography," Biomed. Opt. Express **9**, 3354–3372 (2018).